ELSEVIER

Computational Materials Science 12 (1998) 39–56

COMPUTATIONAL MATERIALS SCIENCE

A computational study of interfacial debonding damage in fibrous composite materials

P. Wriggers *, G. Zavarise [1], T. I. Zohdi

Technische Hochschule Darmstadt, Institut für Mechanik, Hochschulstrasse 1, D-64289 Darmstadt, Germany

Received 6 April 1998; accepted 22 May 1998

Abstract

In this paper the effect of finite interface strength, and possible debonding, on the macroscopic response of a sample of fiber-reinforced composite material is computationally investigated via the finite element method. The sample consists of several fibers embedded in a homogeneous matrix, aligned in the longitudinal direction, and randomly distributed in the transverse direction. Plane strain conditions are enforced. Both the matrix and the fibers are assumed to behave in a linearly elastic manner. The approach is to employ unilateral constraints to model interface strength limits. However, because the debonded surfaces are unknown a priori, and depend on the internal fields, the originally linear elastic problem becomes nonlinear, and hence it must be solved in an iterative manner. Accordingly, a nested contact algorithm scheme is developed, based on an active set strategy, to efficiently simulate multiple interacting unilateral constraints. The nesting allows the nonlinear problem within a Newton step to be transformed into a sequence of linear sub-problems. Using the algorithm, numerical tests are performed on a widely used Aluminum/Boron fiber-reinforced composite combination to determine the effects of debonding on changes in macroscopic responses as a function of interface strength and loading. It is shown that the amount of debonded surface area correlates perfectly with the loss in the macroscopic stiffness of the material. This result lends credence to damage evolution laws, for homogenized material models, which employ interface separation surface area as the primary internal damage variable.

Keywords: Fiber-reinforced composites; Damage; Debonding; Contact formulation; Finite elements

1. Introduction

The use of composite materials has become important in many modern engineering designs. It is tacitly assumed in the manufacture of such materials that the microstructure remains perfectly bonded. However, in many fiber-reinforced composite materials, interfacial debonding is observed, and macroscopic changes in the aggregate response occur. Usually it is the macroscopic stiffness that is of interest. Typically, the aggregate longitudinal stiffness (parallel to the fibers) is usually not significantly affected, since the stiffness is essentially that of the fibers. However, the aggregate transverse stiffness can be greatly reduced by interfacial debonding.

* Corresponding author. Tel.: +49 6151 16 3174; e-mail: wriggers@newton.mechanik.tu-darmstadt.de
[1] On leave from Dipartimento di Costruzioni e Trasporti, Padova Italy.

0927-0256/98/$ – see front matter
PII: S0927-0256(98)00025-1

Historically, the approach has been to describe this sort of macroscopic damage phenomenologically, by resorting to homogenized material models employing "hereditary" or "evolution" laws. Rather than make an attempt to list the variety of approaches in the literature, we refer the reader to surveys found in Refs. [1–3]. Until relatively recently such approaches were essentially the only choice for an expedient simulation of damage for a fiber-reinforced structure containing a significant number of fibers. Semi-empirical relations are usually developed through expensive laboratory trial and error synthesis. The accuracy of these relations can always be called into question, primarily because they are developed for a finite number of specified tests, which may not exactly correspond to the loading states in a given application. Furthermore, they are usually observed macroscopic responses and therefore are phenomological in character. Obviously, approaches based on evolution laws do not allow direct identification of the true damage.

There have been a number of studies focusing on the debonding of a single interface based on idealized models using a flexible "interface" approach. The first of such models seems to be that of Jones and Whittier [4]. Their approach was to represent imperfect bonding by a thin elastic film having shear stress that was dependent on the relative tangential displacement at the interface, while the normal bond stress was proportional to the normal displacement. This approach has been adopted in numerical simulations designed to study failure of the interface. One of the first of such studies was performed by Owen and Lyness [5], who employed a special finite element that allowed shear failure at a predetermined stress, followed by sliding. Similar approaches have been followed by Curiskis and Valliappan [6], Winsom [7] and Nutt and Needleman [8]. Common to these approaches is that when some critical criteria is met on the interface, then the finite element nodes are released. The criteria can generally be described by

$$\text{if } \mathscr{F}(\boldsymbol{\sigma}(\boldsymbol{x})) \geqslant 0 \Rightarrow \text{ debond} \quad \boldsymbol{x} \in \text{ interface}, \tag{1}$$

where $\mathscr{F}$ can be selected in a variety of ways, depending on the complexity of the model used, and the effect to be investigated. It is the main objective of this paper to use this type approach, for *multiple fibers*, to determine the effect of finite interface strength, and hence possible debonding, on the macroscopic response of a sample of fiber-reinforced composite material.

1.1. Scope of this work

In this paper we focus on determining the aggregate transverse response of fiber-reinforced composites, *with finite interface strength*, in the plane strain condition. The fibers are aligned in the longitudinal direction, and randomly distributed in the transverse plane (Fig. 1). The approach taken in this paper is to directly compute the internal fields for a large group of fibers, with no model reduction or assumptions on the internal fields, in order to determine the effects of finite fiber/matrix interface strengths on the macroscopic response. A main quantity of interest is the relation between averages, $\boldsymbol{E}^*$ (denoted RBA), $\langle\boldsymbol{\sigma}\rangle \stackrel{\text{def}}{=} \boldsymbol{E}^* : \langle\boldsymbol{\epsilon}\rangle$, where $\langle\cdot\rangle \stackrel{\text{def}}{=} 1/|\Omega| \int_\Omega \cdot \, \mathrm{d}\boldsymbol{x}$, and where $\boldsymbol{\sigma}$ and $\boldsymbol{\epsilon}$ are the stress and strain tensor fields within a statistically representative sample of material. In our analysis, the RBA tensor, $\boldsymbol{E}^*$, is post processed from our direct computations and provides the following relevant measure of the aggregate damage:

$$\mathscr{D}_{E^*_{ijkl}} = \frac{|E^{*\mathrm{pb}}_{ijkl} - E^{*\mathrm{db}}_{ijkl}|}{|E^{*\mathrm{pb}}_{ijkl}|} \quad 1 \leqslant i,j,k,l \leqslant 3 \ \text{(normalized macroscopic damage)} \tag{2}$$

where pb stands for perfectly bonded, and db stands for a microstructure with possible debonding. For the RBA measure to make sense, i.e. for the RBA tensor to stabilize, the sample size may have to be quite large, possibly containing a significant number of fibers. To give an idea of the geometries under consideration, the fibers (boron in the examples to come later) have a cross-sectional diameter of 8 μm (0.000008 m), while the sample sizes are in the range of approximately $(100\ \mu\mathrm{m})^2$ to $(200\ \mu\mathrm{m})^2$, containing between 50–250 fibers. The fact that the sample must contain a significant amount of microstructure makes computations,

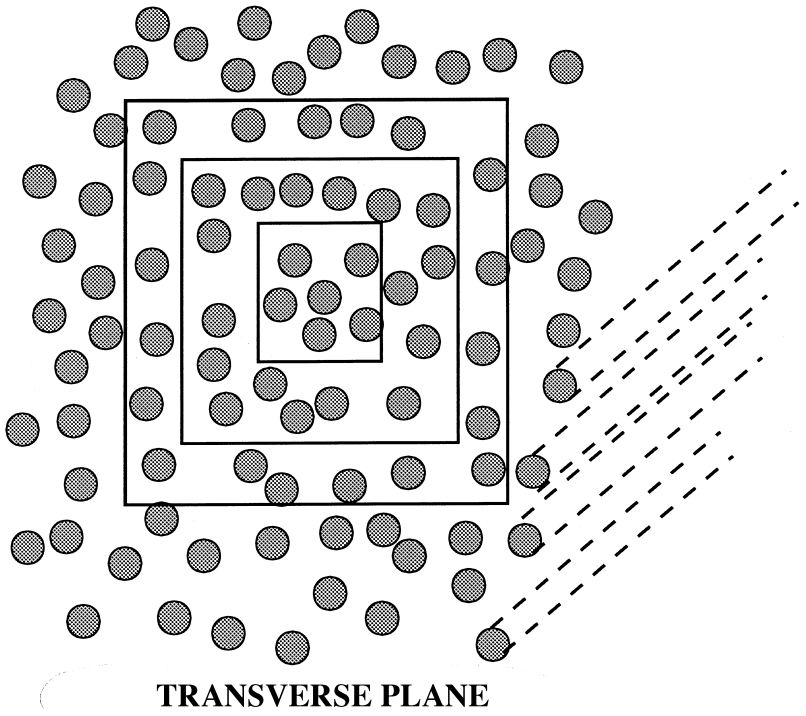

Fig. 1. A selection of fiber groups of increasingly larger sizes.

of even a perfectly bonded material, extremely complex and costly. Primarily, this occurs because when employing numerical methods, such as the finite element, the distance between discretization nodes must be far smaller than the microstructural oscillations to obtain accurate approximate solutions. This has made, until relatively recently, direct numerical simulations involving complex microstructure virtually impossible. Obviously, due to multiple unknown (a priori) contact surfaces, the simulation of solid bodies with debonded interfaces is computationally even more involved relative to the perfectly bonded case.

In order to deal with these difficulties a high performance contact algorithm is developed for rapid multiple fiber debonding simulations. The adopted geometrical contact formulation is based on a well-known node-to-segment algorithm found in Ref. [9], with a modified tangential form found in Ref. [10]. Using this framework, a nested contact algorithm scheme is developed, based on an active set strategy, to efficiently simulate multiple interacting unilateral constraints. The nesting allows the nonlinear problem within a Newton step to be transformed into a sequence of linear sub-problems. Employing the algorithm, numerical tests are performed on a widely used Aluminum/Boron fiber-reinforced composite combination to determine the effects of debonding on changes in macroscopic responses as a function of interface strength and loading. With such a computational tool in hand, one can reduce the number of laboratory experiments needed. The primary advantage is that one can study the effects of quantities such as interface strength and debonded contact area, which are not easily accessible in the laboratory setting, in a very fast, and inexpensive, manner.

The outline of the paper is as follows. In Section 2 basic relations are presented for the measure of the simulated macroscopic response. In Section 3 a contact algorithm is developed which is suitable for multiple debonding surfaces. In Section 4 numerical experiments are given addressing such issues such as mesh dependency, sample size, and, finally, interface strength's effect on damaged responses. Finally in Section 5

a summary is presented. In order to illustrate that such computations are, more or less, accessible in modest, but modern, academic setting, all computations are restricted to a single standard RISC-6000 workstation.

2. Basic relations

We consider a structure composed of linearly elastic material which occupies an open bounded domain in $\Omega \in \mathbb{R}^3$. Its boundary is denoted $\partial\Omega$. The body is in static equilibrium possibly under the action of body forces, $\boldsymbol{f}$, or surface tractions, $\boldsymbol{t}$. The boundary $\partial\Omega$ consists of a portion Γ_u on which the displacements, $\boldsymbol{d}$, are prescribed, and a part Γ_t on which tractions, $\boldsymbol{t}$, are prescribed. The pointwise material is characterized by $\boldsymbol{E}$, a fourth rank linear elasticity tensor with the usual symmetries and positive definite requirements. The components of $\boldsymbol{E}$ are functions of spatial position in the body. Throughout the analysis, small deformations are assumed, where $\boldsymbol{\sigma}$ and $\boldsymbol{\epsilon}$ denote the stress and (infinitesimal) strain tensor fields in the body, related by $\boldsymbol{\sigma} = \boldsymbol{E}:\boldsymbol{\epsilon}$. In general, our selected measure of the macroscopic response, $\boldsymbol{E}^*$ is not a material property, i.e. it is a relation between averages.

The usual procedure is to specify a set of six linearly independent loadings on the sample boundary, either of uniform strain or uniform stress type. These loadings are, in a sense, similar to those that would be performed on a laboratory test specimen. For a detailed discussion see Ref. [11]. Each loading state provides explicit computation of six components of $\boldsymbol{E}^*$. In the past, primarily because of insufficient computational power, analytical methods have been developed which bound, above and below, the macroscopic response of a sample in terms of only physical data such as the volume fractions and elastic properties of the constituents. Surveys can be found in Refs. [11,12]. However, a universal requirement of these classical results is perfectly bonded interfaces, thus making these results inapplicable to the debonded regimes considered in this study. However, towards the end of this paper we make some further comments on this issue.

2.1. Direct computation

Explicitly, to determine $\boldsymbol{E}^*$, one specifies six linearly independent loading of the form, (1) $\boldsymbol{u}|_{\partial\Omega} = \boldsymbol{S}\cdot\boldsymbol{x}$ or (2) $\boldsymbol{t}|_{\partial\Omega} = \boldsymbol{T}\cdot\boldsymbol{n}$ where $\boldsymbol{S}$ and $\boldsymbol{T}$ are symmetric second order strain and stress tensors, with spatially constant components. Each independent loading state provides six equations, for a total of 36, which are used to determine the relation between average (the RBA tensor) stress and strain

$$\begin{bmatrix} \langle\sigma_{11}\rangle_\Omega \\ \langle\sigma_{22}\rangle_\Omega \\ \langle\sigma_{33}\rangle_\Omega \\ \langle\sigma_{12}\rangle_\Omega \\ \langle\sigma_{23}\rangle_\Omega \\ \langle\sigma_{13}\rangle_\Omega \end{bmatrix} = \begin{bmatrix} E^*_{1111} & E^*_{1122} & E^*_{1133} & E^*_{1112} & E^*_{1123} & E^*_{1113} \\ E^*_{2211} & E^*_{2222} & E^*_{2233} & E^*_{2212} & E^*_{2223} & E^*_{2213} \\ E^*_{3311} & E^*_{3322} & E^*_{3333} & E^*_{3312} & E^*_{3323} & E^*_{3313} \\ E^*_{1211} & E^*_{1222} & E^*_{1233} & E^*_{1212} & E^*_{1223} & E^*_{1213} \\ E^*_{2311} & E^*_{2322} & E^*_{2333} & E^*_{2312} & E^*_{2323} & E^*_{2313} \\ E^*_{1311} & E^*_{1322} & E^*_{1333} & E^*_{1312} & E^*_{1323} & E^*_{1313} \end{bmatrix} \begin{bmatrix} \langle\epsilon_{11}\rangle_\Omega \\ \langle\epsilon_{22}\rangle_\Omega \\ \langle\epsilon_{33}\rangle_\Omega \\ 2\langle\epsilon_{12}\rangle_\Omega \\ 2\langle\epsilon_{23}\rangle_\Omega \\ 2\langle\epsilon_{13}\rangle_\Omega \end{bmatrix}. \tag{3}$$

The usual choices for the six independent load cases are

$$\boldsymbol{S} \text{ or } \boldsymbol{T} = \begin{bmatrix} \beta & 0 & 0 \\ 0 & 0 & 0 \\ 0 & 0 & 0 \end{bmatrix}, \begin{bmatrix} 0 & 0 & 0 \\ 0 & \beta & 0 \\ 0 & 0 & 0 \end{bmatrix}, \begin{bmatrix} 0 & 0 & 0 \\ 0 & 0 & 0 \\ 0 & 0 & \beta \end{bmatrix}, \begin{bmatrix} 0 & \beta & 0 \\ \beta & 0 & 0 \\ 0 & 0 & 0 \end{bmatrix}, \begin{bmatrix} 0 & 0 & 0 \\ 0 & 0 & \beta \\ 0 & \beta & 0 \end{bmatrix}, \begin{bmatrix} 0 & 0 & \beta \\ 0 & 0 & 0 \\ \beta & 0 & 0 \end{bmatrix}, \tag{4}$$

where β is a load parameter. If the RBA response is assumed isotropic then only one test loading, containing nonzero dilatational and deviatoric components, is necessary to determine the RBA bulk and shear moduli:

$$\left\langle \frac{\operatorname{tr}\boldsymbol{\sigma}}{3} \right\rangle = 3\kappa^* \left\langle \frac{\operatorname{tr}\epsilon}{3} \right\rangle \quad \text{and} \quad \langle \boldsymbol{\sigma}' \rangle = 2\mu^* \langle \boldsymbol{\epsilon}' \rangle. \tag{5}$$

Defining

$$\boldsymbol{E}^*_{11} \stackrel{\text{def}}{=} \begin{pmatrix} E^*_{1111} \\ E^*_{1122} \\ E^*_{1133} \\ E^*_{1112} \\ E^*_{1123} \\ E^*_{1113} \end{pmatrix}, \quad \boldsymbol{E}^*_{22} \stackrel{\text{def}}{=} \begin{pmatrix} E^*_{2211} \\ E^*_{2222} \\ E^*_{2233} \\ E^*_{2212} \\ E^*_{2223} \\ E^*_{2213} \end{pmatrix} \text{...etc.} \qquad \langle \boldsymbol{\sigma}^{(K)} \rangle \stackrel{\text{def}}{=} \begin{pmatrix} \langle \sigma^{(K)}_{11} \rangle_\Omega \\ \langle \sigma^{(K)}_{22} \rangle_\Omega \\ \langle \sigma^{(K)}_{33} \rangle_\Omega \\ \langle \sigma^{(K)}_{12} \rangle_\Omega \\ \langle \sigma^{(K)}_{23} \rangle_\Omega \\ \langle \sigma^{(K)}_{13} \rangle_\Omega \end{pmatrix}, \quad \langle \boldsymbol{\epsilon}^{(K)} \rangle \stackrel{\text{def}}{=} \begin{pmatrix} \langle \epsilon^{(K)}_{11} \rangle_\Omega \\ \langle \epsilon^{(K)}_{22} \rangle_\Omega \\ \langle \epsilon^{(K)}_{33} \rangle_\Omega \\ \langle \epsilon^{(K)}_{12} \rangle_\Omega \\ \langle \epsilon^{(K)}_{23} \rangle_\Omega \\ \langle \epsilon^{(K)}_{13} \rangle_\Omega \end{pmatrix}, \tag{6}$$

where, for example, $K = \mathrm{I}, \mathrm{II}, \ldots, \mathrm{VI}$, refer to the first test loading, the second test loading... etc, and $11, 22 \ldots$ etc stand for the row of the elasticity tensor. For the general case, the system generated by the six loading cases that must be solved is:

$$\underbrace{\begin{bmatrix} \langle \mathscr{E}^{(\mathrm{I})} \rangle_\Omega \\ \langle \mathscr{E}^{(\mathrm{II})} \rangle_\Omega \\ \langle \mathscr{E}^{(\mathrm{III})} \rangle_\Omega \\ \langle \mathscr{E}^{(\mathrm{IV})} \rangle_\Omega \\ \langle \mathscr{E}^{(\mathrm{V})} \rangle_\Omega \\ \langle \mathscr{E}^{(\mathrm{IV})} \rangle_\Omega \end{bmatrix}}_{36\times 36} \underbrace{\begin{bmatrix} E^*_{11} \\ E^*_{22} \\ E^*_{33} \\ E^*_{12} \\ E^*_{13} \\ E^*_{23} \end{bmatrix}}_{36\times 1} = \underbrace{\begin{bmatrix} \langle \sigma^{(\mathrm{I})} \rangle_\Omega \\ \langle \sigma^{(\mathrm{II})} \rangle_\Omega \\ \langle \sigma^{(\mathrm{III})} \rangle_\Omega \\ \langle \sigma^{(\mathrm{IV})} \rangle_\Omega \\ \langle \sigma^{(\mathrm{V})} \rangle_\Omega \\ \langle \sigma^{(\mathrm{VI})} \rangle_\Omega \end{bmatrix}}_{36\times 1} \tag{7}$$

where

$$\langle \mathscr{E}^{(K)} \rangle \stackrel{\text{def}}{=} \underbrace{\begin{bmatrix} \langle \epsilon^{(K),\mathrm{T}} \rangle_\Omega & O^{\mathrm{T}} & O^{\mathrm{T}} & O^{\mathrm{T}} & O^{\mathrm{T}} & O^{\mathrm{T}} \\ O^{\mathrm{T}} & \langle \epsilon^{(K),\mathrm{T}} \rangle_\Omega & O^{\mathrm{T}} & O^{\mathrm{T}} & O^{\mathrm{T}} & O^{\mathrm{T}} \\ O^{\mathrm{T}} & O^{\mathrm{T}} & \langle \epsilon^{(K),\mathrm{T}} \rangle_\Omega & O^{\mathrm{T}} & O^{\mathrm{T}} & O^{\mathrm{T}} \\ O^{\mathrm{T}} & O^{\mathrm{T}} & O^{\mathrm{T}} & \langle \epsilon^{(K),\mathrm{T}} \rangle_\Omega & O^{\mathrm{T}} & O^{\mathrm{T}} \\ O^{\mathrm{T}} & O^{\mathrm{T}} & O^{\mathrm{T}} & O^{\mathrm{T}} & \langle \epsilon^{(K),\mathrm{T}} \rangle_\Omega & O^{\mathrm{T}} \\ O^{\mathrm{T}} & O^{\mathrm{T}} & O^{\mathrm{T}} & O^{\mathrm{T}} & O^{\mathrm{T}} & \langle \epsilon^{(K),\mathrm{T}} \rangle_\Omega \end{bmatrix}}_{6\times 36} \tag{8}$$

where $\boldsymbol{O}^{\mathrm{T}} \stackrel{\text{def}}{=} \{0,0,0,0,0,0\}$.

2.2. Finite interface strength

We treat the interface strength between the fiber and matrix as a parameter, a scalar multiple of the yield strength of the matrix material:

$$\frac{\sigma^{\text{Y-interface}}}{\sigma^{\text{Y-matrix}}} = \mathscr{Y}. \tag{9}$$

The critical loadings considered are the maximum of the normal stress, and the tangential stress on the interface

$$t_n \overset{\text{def}}{=} |\boldsymbol{n}\cdot\boldsymbol{\sigma}\cdot\boldsymbol{n}|, \quad t_a \overset{\text{def}}{=} |\boldsymbol{n}\cdot\boldsymbol{\sigma}\cdot\boldsymbol{a}|, \quad \boldsymbol{n}\cdot\boldsymbol{a}=0, \quad \boldsymbol{n}\cdot\boldsymbol{n}=1, \quad \boldsymbol{a}\cdot\boldsymbol{a}=1, \tag{10}$$

where $\boldsymbol{n}$ and $\boldsymbol{a}$ are the unit normal and unit tangent respectively. The criteria to debond is

$$\max(t_n, t_a) \geqslant \sigma^{\text{Y-interface}} \Rightarrow \text{ debond.} \tag{11}$$

Essentially, the test procedure for a given loading β, sample size Ω, and interface strength via $\mathscr{Y}$ is to solve associated boundary value problem and post process the solution to obtain $\boldsymbol{E}^{*\text{db}}$. *In all of the simulations in this paper, we allow interfacial failure only in tension.*

3. A contact formulation for imperfect bonding

The debonding process within the microstructural simulations is modelled by a contact formulation which can handle adhesional forces up to a prescribed tensile limit on the contact interface. We assume perfect stick, i.e. no sliding when in contact, throughout the analysis. To derive the associated contact formulation, we first consider one fiber cross-section Ω_α within the matrix material Ω_0 (see Fig. 2). The classical penalty method is used to enforce the contact constraints. Following the notation in Ref. [13] we define the kinematic nonpenetration condition by a gap function g_{N}. Fig. 2 shows, for the two-dimensional case the initial and deformed configuration of one fiber cross-section, Ω_α, and the matrix, Ω_0. The entire body is given by $\Omega \overset{\text{def}}{=} \Omega_0 \cup_{\alpha=1}^{N} \overline{\Omega_\alpha}$, where N is the number of fibers. Since there is no initial gap in the undeformed state we can compute the gap between the bodies from the displacement fields $\boldsymbol{u}^\alpha$ and $\boldsymbol{u}^0$. The normal vector $\boldsymbol{n}^0$ is associated with the master body Ω_0 which represents the matrix material.

Assuming that the contact boundary locally describes a convex region, one can relate to every point on Γ^α a point on Γ^0 via the minimal distance problem

$$\|\boldsymbol{u}^\alpha - \bar{\boldsymbol{u}}^0\| \overset{\text{def}}{=} \min\ d^0(\xi) = \min_{\boldsymbol{u}^0 \subseteq \Gamma^0} \|\boldsymbol{u}^\alpha - \boldsymbol{u}^0(\xi)\|, \tag{12}$$

where ξ denotes the parametrization of the displacement field $\boldsymbol{u}^0$ on the boundary Γ^0. The minimization process yields the condition $(\boldsymbol{u}^\alpha - \bar{\boldsymbol{u}}^0)\cdot\bar{\boldsymbol{a}}^0 = 0$ which means that $(\boldsymbol{u}^\alpha - \bar{\boldsymbol{u}}^0)$ points in the direction of $\bar{\boldsymbol{n}}^0$. Now

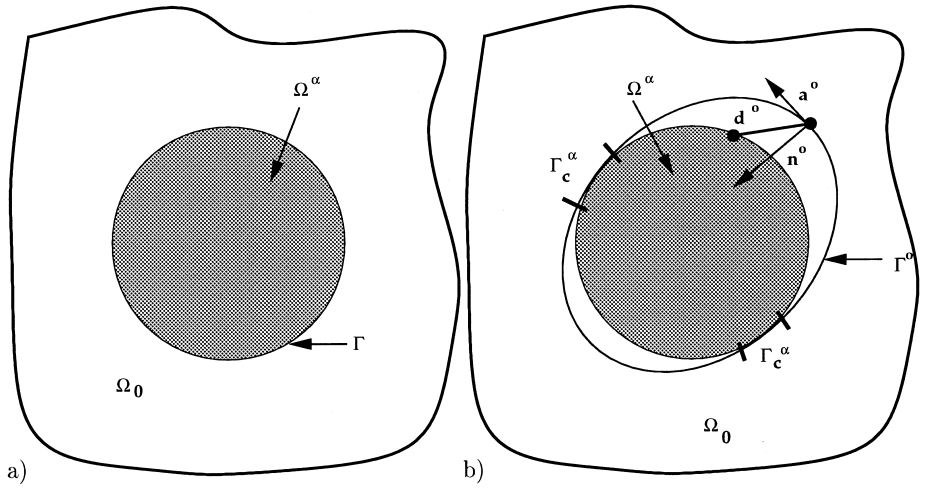

Fig. 2. (a) One fiber cross-section Ω_α within the matrix material Ω_0. (b) Definition of the gap for one fiber cross-section.

we may write the geometrical contact constraint inequality which prevents penetration of one body into the other

$$g_{\mathrm{N}} = (\boldsymbol{u}^{\alpha} - \bar{\boldsymbol{u}}^{0}) \cdot \bar{\boldsymbol{n}}^{0} \geqslant 0. \tag{13}$$

In view of the penalty formulation, which will be applied to solve the contact problems, we introduce a penetration function since the method allows a small penetration in $\Gamma_{\mathrm{c}}^{\alpha}$:

$$g_{\mathrm{N}}^{-} = \begin{cases} (\boldsymbol{u}^{\alpha} - \bar{\boldsymbol{u}}^{0}) \cdot \bar{\mathbf{n}}^{0} & \text{if } (\boldsymbol{u}^{\alpha} - \bar{\boldsymbol{u}}^{0}) \cdot \bar{\boldsymbol{n}}^{0} < 0, \\ 0 & \text{otherwise.} \end{cases} \tag{14}$$

The stick condition is a purely kinematic constraint condition which prohibits relative tangential displacement within the contact surface. This means that a point on $\Gamma_{\mathrm{c}}^{\alpha}$ does not move relative to the surface and thus keeps its position at $\bar{\xi}$. We have the constraint condition

$$g_{\mathrm{T}} = (\boldsymbol{u}^{\alpha} - \bar{\boldsymbol{u}}^{0}) \cdot \bar{\boldsymbol{a}}^{0} = 0. \tag{15}$$

With these geometrical relations the weak form of the contact contributions can be formulated for each fiber cross-section Ω_{α} ($\epsilon_{\mathrm{N}} > 0, \epsilon_{\mathrm{T}} > 0$)

$$G_{\mathrm{c}}^{\alpha}(\boldsymbol{u}^{\alpha}, \boldsymbol{u}^{0}) = \int_{\Gamma_{\mathrm{c}}^{\alpha}} (\epsilon_{N} g_{\mathrm{N}}^{-} \delta g_{\mathrm{N}}^{-} + \epsilon_{T} g_{T} \delta g_{\mathrm{T}}) \, \mathrm{d}\gamma, \tag{16}$$

where the variations of the normal and tangential gap are given by

$$\delta g_{\mathrm{N}} = (\boldsymbol{w}^{\alpha} - \bar{\boldsymbol{w}}^{0}) \cdot \boldsymbol{n}, \quad \delta g_{\mathrm{T}} = (\boldsymbol{w}^{\alpha} - \bar{\boldsymbol{w}}^{0}) \cdot \boldsymbol{a}^{o}, \tag{17}$$

where the $\boldsymbol{w}$'s are the appropriate variations or test functions [13]. The normal contact stress t_{N} on the contact interface $\Gamma_{\mathrm{c}}^{\alpha}$, needed for the computation of the adhesional interface law, is computed via $t_{\mathrm{N}} = \epsilon_{\mathrm{N}} g_{\mathrm{N}}^{-}$. The entire formulation is given by the following virtual work formulation:

Find a $\boldsymbol{u}^{\mathrm{db}}, \boldsymbol{u}^{\mathrm{db}}|_{\Gamma_u} = \boldsymbol{d}$, such that $\forall \boldsymbol{w}^{\alpha}, \boldsymbol{w}$ such that $\boldsymbol{w}^{\alpha}|_{\Gamma^{\alpha}} = \boldsymbol{w}|_{\Gamma^{\alpha}}$

$$\int_{\Omega} \nabla \boldsymbol{w} : \boldsymbol{E} : \nabla \boldsymbol{u}^{\mathrm{db}} \, \mathrm{d}\boldsymbol{x} + \sum_{\alpha=1}^{N} \int_{\Omega_{\alpha}} \nabla \boldsymbol{w}^{\alpha} : \boldsymbol{E} : \boldsymbol{u}^{\alpha \mathrm{db}} \, \mathrm{d}\boldsymbol{x} = \int_{\Omega} \boldsymbol{f} \cdot \boldsymbol{w} \, \mathrm{d}\boldsymbol{x} + \int_{\Gamma_t} \boldsymbol{t} \cdot \boldsymbol{w} \, \mathrm{d}s + \sum_{\alpha=1}^{N} G_{\mathrm{c}}^{\alpha}. \tag{18}$$

A main difficulty with the analysis, stemming from the contact constraints, is that the debonded surfaces are unknown a priori, and the corresponding boundary value formulation must be solved in an iterative manner. Correspondingly, discretization and linearizations of the quantities in Eq. (18) are needed for the finite element formulation of the penalty method utilizing the Newton–Raphson scheme to solve the contact problem. The explicit formulation of these expressions can be found for a linear node-to-segment discretization in Refs. [9,10,13]. A nested scheme, based on an active set strategy, that checks the gap status outside the Newton loop has been specifically developed for this class of problems. The nesting allows the nonlinear problem within the step to be transformed into a sequence of linear sub-problems. The corresponding algorithm is as follows.

Initially assume bonding on all interfaces ($g_{\mathrm{N}} = 0, g_{\mathrm{T}} = 0$)
LOOP: DO $i = 1, \ldots$ *CONVERGENCE*
  LOOP over all surfaces Γ^{α}
    LOOP over all segments s at interface Γ^{α}
      Step a: *Check for debonding and contact in s*
      Step b: *IF* $g_{\mathrm{N}_s} > \bar{t}_{\mathrm{N}_s}^{\alpha} \Rightarrow$ *change state to no contact*
      Step c: *IF* $g_{\mathrm{N}_s} \leqslant 0 \Rightarrow$ *change state to contact*

END LOOP s
END LOOP Γ^{α}
LOOP: DO $j = 1, \ldots$ *CONVERGENCE*
Compute global solution from equation (18)
END LOOP j
Check for convergence
IF no contact elements have changed state $\Rightarrow$ *STOP*
END LOOP i

4. Numerical experiments

Numerical tests were carried out by adding special purpose features to the basic finite element code FEAP (courtesy of Prof. R.L. Taylor). Standard two-dimensional isoparametric plane-strain bilinear elements were used for the continuum descritization. The material data used is shown in Table 1. Following the usual procedure, along the contact surfaces (interface boundaries between the matrix and the fibers) the nodes have been duplicated. To calibrate the testing procedure, we performed a series of preliminary tests. These tests were used to determine adequate sample sizes and finite element mesh densities for realistic and accurate simulations.

4.1. Preliminary tests

It was initially unclear whether there was any significant interaction between the fibers, thus raising the possibility that we could use an approximate, computationally inexpensive, analytical or semi-analytical method based on limited mutual fiber interaction. However, we found this not to be the case for the class of problems under consideration. To illustrate the need for computing the interaction of the fibers, we performed a series of preliminary tests. First, a single fiber occupying 46% volume fraction was embedded in an appropriate square matrix material (volume fraction 54%). Displacement-controlled load cases were considered:

$$\underbrace{\boldsymbol{u}|_{\partial\Omega} = \begin{bmatrix} 0.001 & 0 \\ 0 & 0 \end{bmatrix} \begin{bmatrix} x_1 \\ x_2 \end{bmatrix}}_{\stackrel{\text{def}}{=}\text{TEN-TEST}} \qquad \underbrace{\boldsymbol{u}|_{\partial\Omega} = \begin{bmatrix} 0 & 0.0005 \\ 0.0005 & 0 \end{bmatrix} \begin{bmatrix} x_1 \\ x_2 \end{bmatrix}}_{\stackrel{\text{def}}{=}\text{SII-TEST}} \tag{19}$$

Also combined loading was considered. Afterwards, the same loadings were applied to a sample with the same relative volume fraction containing a periodic cubic 9×9 fiber arrangement (81 total). We then isolated the solution around the center fiber of the 9×9 arrangement, and compared it to the single fiber solution (Fig. 3), for each individual loading. Figs. 4 and 5 illustrate the solutions, and their completely different character for uniform shear loading. The results were similar for the other loading states. These simple examples gave us an intuitive motivation for computations that consider group interactions, such as

Table 1
Material data for the composite simulation

Material	Vol. Frac.	κ (GPa)	μ (GPa)
FIBER:Boron	46%	230	172
MATRIX:6061 Aluminum	54%	67.5	25.9

Yield stress for Aluminum is approximately 40 (GPa).

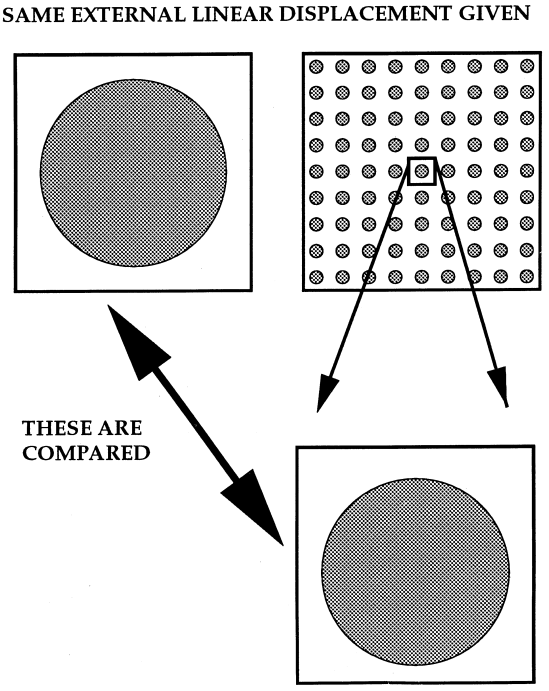

Fig. 3. Comparison for a single fiber and multiple fiber comparison.

a direct FEM computation, important. Clearly, the fibers do interact, and the use of methods, such as dilute methods, based upon limited interactions, would be unreliable.

A second important issue was to determine how large a sample is needed to provide a stable RBA tensor. With this in mind, we systematically increased the sample size until we computed no change in the macroscopic response. This was performed initially with the perfectly bonded microstructure. In an attempt to make the simulations realistic, a degree of error is given in the fiber placement, as there would be in a true composite. Accordingly, the unit square area was divided into $N \times N$ sub-squares of equal area. Each fiber cross-section was moved randomly in the transverse direction, however, restricted to remain within the corresponding sub-square (Fig. 6). The macroscopic moduli (the RBA tensor) of such an arrangement is approximately transversely isotropic. For an $N \times N$ fiber arrangement, the previously mentioned linear displacement loadings were applied. The geometric microstructure corresponded to the 0.000008 m in diameter Boron fibers embedded in the Aluminum matrix, previously referred to in the beginning of the paper. When the TEN-TEST is applied one can determine the RBA transverse bulk modulus, κ^*, and when the SH-TEST is applied one can determine the RBA transverse shear modulus, μ^*. In order to consider a general loading, we employed the combined loading and proceeded with a sequence of perfectly bonded microstructures 1×1, 2×2, 4×4, etc. (fiber arrangements "randomly" positioned) until we measured no more change (to an appreciable error, which we set to $\approx 1\%$) in the transverse bulk κ^* and transverse shear μ^* moduli for three successive RBA tensors. [2] It was found that macroscopic response stabilized starting with the fiber sequence 8×8, 12×12, 16×16. This was repeated, for finite interface strength (allowing debonding), with sample stabilization occurring for a similar number of fibers (Table 2).

[2] The macroscopic response was assumed to be transversely isotropic.

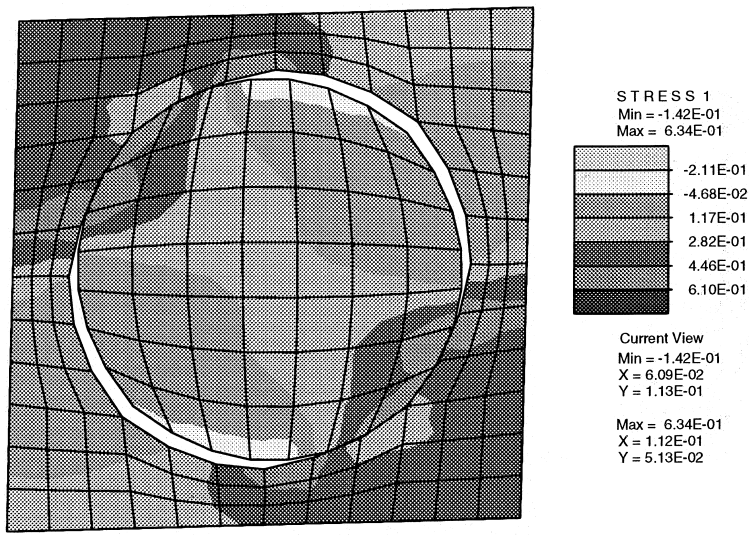

Fig. 4. (SH-TEST) One fiber with a uniform loading on the cell boundary.

The final issue in the preliminary tests was to determine adequate meshes for the 8×8 fiber microstructure (Table 3). The mesh dependency was checked by varying the mesh density. It was found that a minimum of 12×12 elements per fiber were needed for mesh-independent results to a tolerable error. This tolerable error was defined as no more than a 1% relative difference in the successive RBA tensor's transverse moduli. The practical conclusion of our somewhat preliminary experiments was that, *for this composite combination*, at least an 8×8 fiber arrangement with at least a 12×12 element/fiber mesh density (approximately 23 500 numerical degrees of freedom total) was required for a statistically stable sample with tolerable mesh dependency. The original and deformed meshes for the 8×8 arrangement are shown

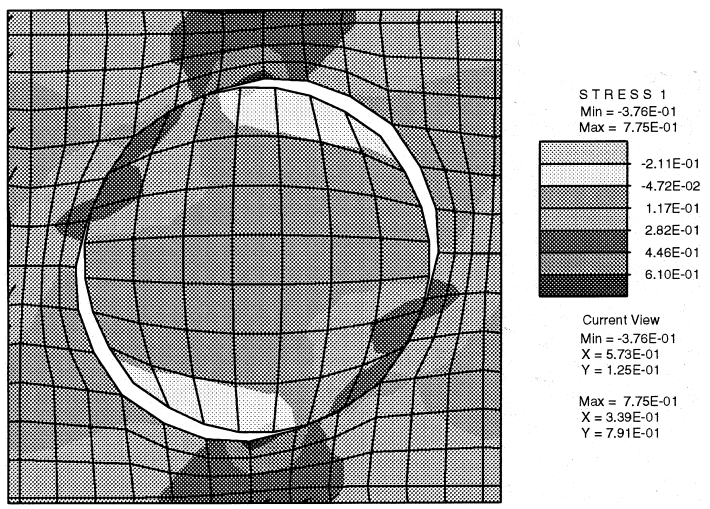

Fig. 5. (SH-TEST) An extracted center cell solution (from a 9×9 arrangement).

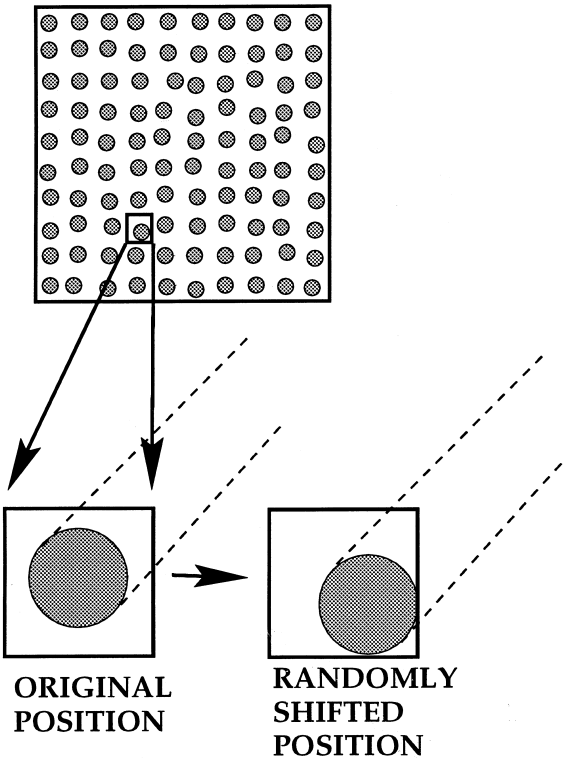

Fig. 6. Fiber placement for numerical tests.

(for the combined loading) in Figs. 7 and 8. To give an idea of the character of the internal fields, the Mises stress for a 16×16 fiber microstructure with combined linear displacement loading is given in Fig. 9.

4.2. Losses in macroscopic strength due to debonding

4.2.1. Nonincrementally loaded tests

The test of primary interest for losses in transverse strength is the tension test (TEN-TEST). Responses corresponding to different values of $\sigma^{\text{Y-interface}}$ to generate the interfacial strength are collected in Table 4. The obvious general trend, with increasing interfacial strength, was to make the RBA tensor stiffer. Here,

Table 2
(COMBINED TEN-TEST, SH-TEST): Increasing the mesh density with $\mathscr{Y} = 2$

Arrangement	$(\kappa^*)^{\text{db}}$(GPa)	$(\mu^*)^{\text{db}}$(GPa)	$O\%$	elem/fiber	active DOF
1×1	83.4	29.0	62.3	12×12	326
4×4	82.9	38.4	59.1	12×12	5732
8×8	82.9	39.8	56.7	12×12	23402
12×12	82.0	40.1	57.4	12×12	52950
16×16	82.2	40.6	56.7	12×12	94442

$O\%$ = percent open debonded contact area.

Table 3
(COMBINED TEN-TEST, SH-TEST/8 × 8 fiber arrangement) Increasing the mesh density for perfectly bonded material

$(\kappa^*)^{db}$(GPa)	$(\mu^*)^{db}$(GPa)	elem/fiber	active DOF
102.1	49.1	6 × 6	4 418
103.4	49.5	12 × 12	18 050
103.6	49.6	18 × 18	40 898
103.7	49.6	24 × 24	72 962

one can directly correlate the RBA stiffness with the interface strength. Two important curve-fit relations for behavior of the loss in material stiffness with interface strength for TEN-TEST are:

$$0.906 - 0.152Ln(\sigma^{\text{Y-interface}}) = \mathscr{D}_{\kappa^*} = \%\ \text{lost stiffness} \quad R^2 = 0.99\ (\approx \text{perfect fit}),$$
$$0.002(O\%)^{1.126} = \mathscr{D}_{\kappa^*} = \%\ \text{lost stiffness} \quad R^2 = 1.00(\text{perfect fit}), \tag{20}$$

where $O\%$ is the percent of open debonded fiber contact area, and R^2 is the curve-fit regression value. Compression and shear tests were also performed (also tabulated in Table 4). For the shear case the reduction in strength was mild ranging between 6% and 8% in lost stiffness, since a large portion of the interfaces are in a state of compression. Compression produces insignificant changes for the range of loading we considered. This was, of course, in large part due to the fact that we chose to have interfacial failure only in tension.

4.2.2. Incrementally loaded tests/accumulated damage

The testing procedure was repeated, in an incremental fashion, for TEN-TEST where the damaged interfaces from the previous step were used as the starting point for the next load increment. As one would expect, the stiffness lost is greater than for the corresponding single applied load case (Figs. 10 and 11,

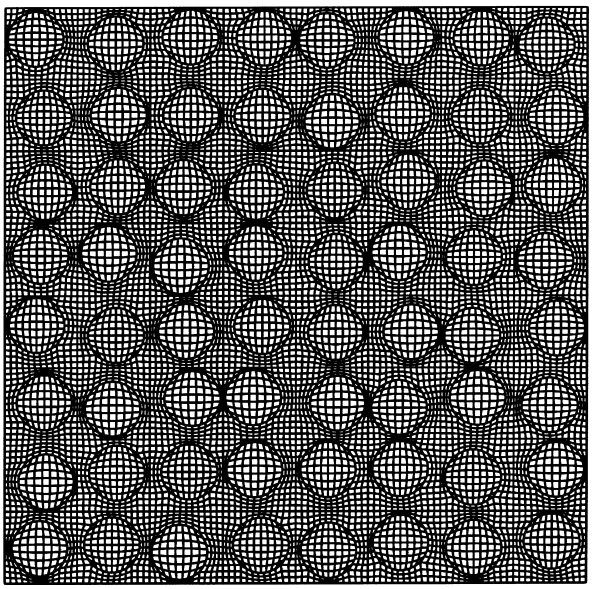

Fig. 7. The mesh used for the 8 × 8 fiber microstructure with 12 × 12 mesh density.

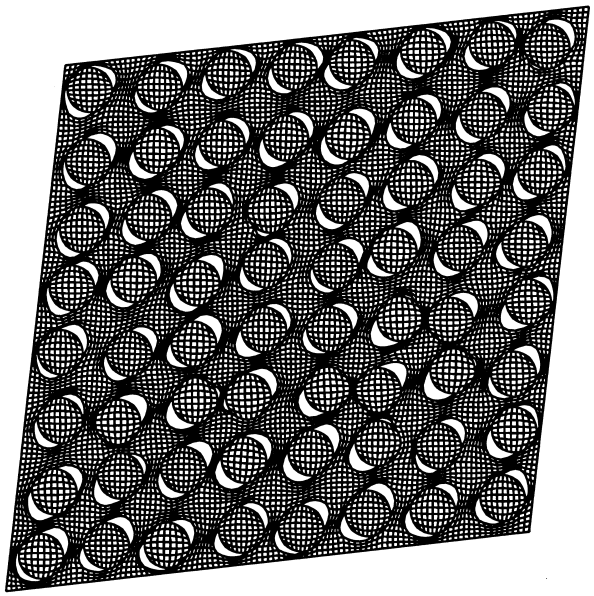

Fig. 8. (SH-TEST) 8×8 fibers with a deformed configuration magnified 500 times.

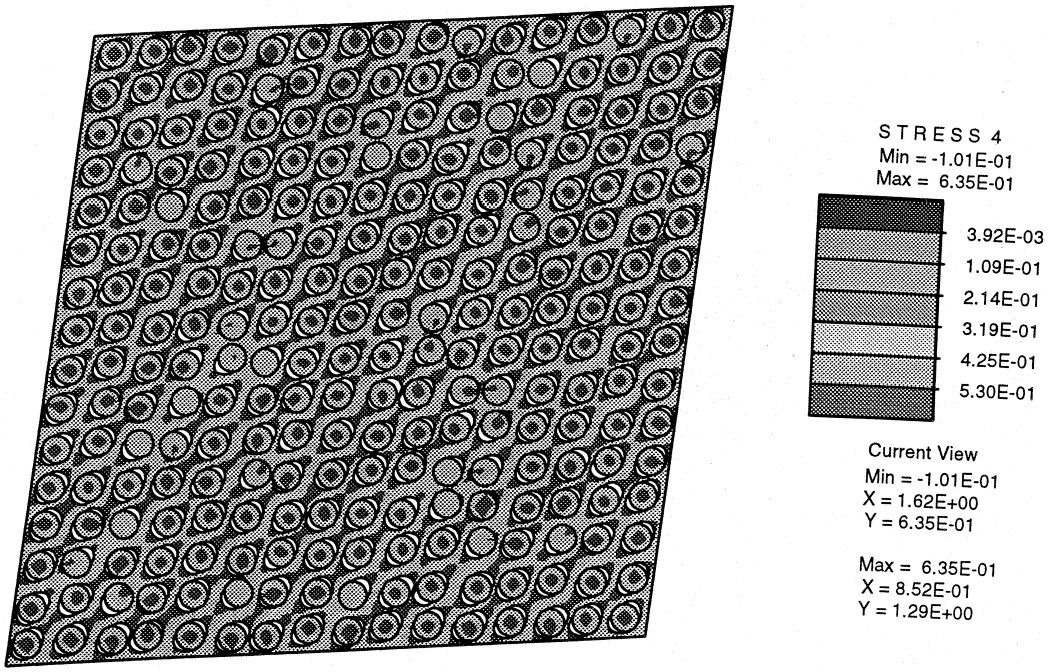

Fig. 9. (COMBINED-TEST) Mises stresses for a 16×16 fiber problem.

Table 4
8×8 (diameter = 0.000008 m) fibers of boron in an aluminum matrix

Test	$\mathscr{Y}$	CP%	CT%	O%	$(\kappa^*)^{db}$(GPa)	$(\mu^*)^{db}$(GPa)	$\mathscr{D}_{\kappa^*}$	$\mathscr{D}_{\mu^*}$
TEN-TEST	1	0.7	1.9	97.5	67.8	––	0.34	––
SH-TEST	1	56.8	21.1	22.1	––	45.6	––	0.08
TEN-TEST	2	0.1	29.8	70.1	78.9	––	0.24	–
SH-TEST	2	54.1	45.3	0.6	––	46.4	––	0.06
TEN-TEST	3.5	0.1	56.8	43.2	89.3	––	0.14	––
SH-TEST	3.5	53.8	46.2	0.0	––	46.6	––	0.06
TEN-TEST	4.5	0.1	61.7	38.2	91.1	––	0.12	––
SH-TEST	4.5	53.8	46.2	0.0	––	46.6	––	0.06
–(TEN-TEST)	1	100.0	0.0	0.0	103.4	––	0.00	––
–(SH-TEST)	1	57.0	22.0	21.0	––	45.7	––	0.08

CP% = percent contact area in compression, CT% = percent contact area in tension but in contact, O% = percent contact area open.

Table 5). The additional losses due to accumulated damage ranged from 5.1% to 12.4%. As one can see from the second plot, the amount of open debonded surface area is an extremely good indicator of the loss in stiffness. There is essentially a linear relationship, independent of interface strength.

4.2.3. Behavior of the classical bounds

The classical Hill–Reuss–Voigt bounds (see Ref. [14] for details) were computed for "effective properties" (loosely speaking hypothetical RBA for an infinitely large sample) against the largest sample that we computed with, a 16×16 fiber arrangement (256 fibers). The bounds are

$$\underbrace{\langle \boldsymbol{E}^{-1} \rangle^{-1}}_{\text{Reuss}} \leqslant \boldsymbol{E}^* \leqslant \underbrace{\langle \boldsymbol{E} \rangle}_{\text{Voigt}}, \tag{21}$$

where this inequality means that the eigenvalues of the tensors $\boldsymbol{E}^* - \langle \boldsymbol{E}^{-1} \rangle^{-1}$ and $\langle \boldsymbol{E} \rangle - \boldsymbol{E}^*$ are nonnegative. *The expression in Eq. (21) is not valid when the microstructure debonds.* However, we checked the bounds

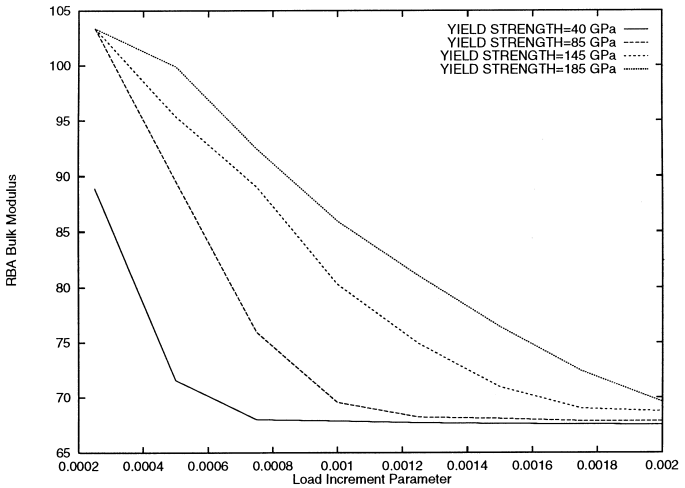

Fig. 10. (TEN-TEST) Progressive loss in the RBA bulk modulus with debonding due to increasing uniaxial loading yield strengths.

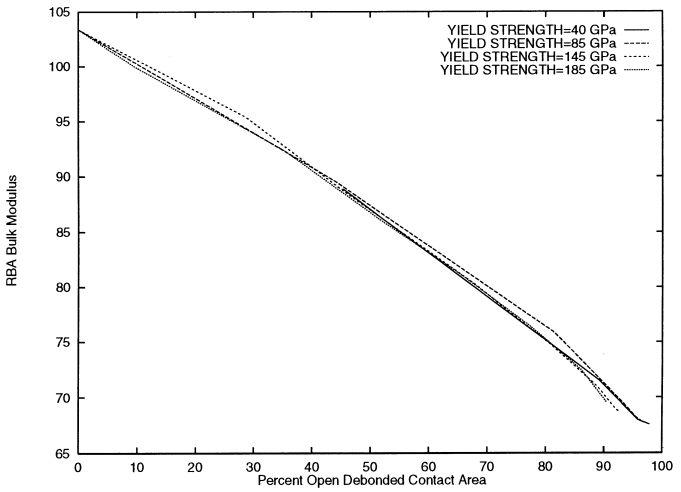

Fig. 11. (TEN-TEST) Bulk moduli versus debonded area due to increasing uniaxial loading for varying interface yield strengths. An approximate linear relationship, valid for all tests can be directly determined to be $\kappa^{*db} = 103.4 - 0.34\ O\%$.

anyway, as shown in Table 6. For example, as one would expect, the computed bulk moduli violated the bounds, except of course in the perfectly bonded cases. Other bounds were checked as well. For example the Hashin–Shtrikman bounds (see Refs. [15,16]), which are, strictly speaking, not applicable because they hold for isotropic effective responses, were violated immediately, and in fact remained invalid even in the perfectly bonded case due to the inherent transverse isotropy in the fibrous material. Bounds, valid for transverse isotropic macroscopic responses [17–19] were also computed, but were violated for virtually all

Table 5
(TEN-TEST/8×8 fiber arrangement/12×12) A comparison between progressive (accumulated) debonded stiffness (incremental loading) and a single static test of the the same final load (displacement controlled $\beta = 0.002$)

$\mathscr{Y}$(GPa)	$(1) = \kappa^{*db}$(GPa)	$(2) = \kappa^{*db}$(GPa)(accum.)	$\frac{(1)-(2)}{(1)} \times 100$
1	67.8	67.8	0
2	78.9	69.1	12.4
3.5	89.3	80.5	9.8
4.5	91.1	86.5	5.1
∞	103.4	103.4	0

Table 6
The effective property bounds for bulk modulus perfectly bonded boron in an aluminum matrix and the RBA bulk moduli for various interface strengths for a 16×16 sample

$\mathscr{Y}$	$\langle\kappa\rangle$(GPa)	$\langle\kappa^{-1}\rangle^{-1}$(GPa)	TEN-TEST: κ^*(GPa)
1	142.25	100.0	67.8
2	142.25	100.0	78.9
3.5	142.25	100.0	89.3
4.5	142.25	100.0	91.1
∞	142.25	100.0	103.4

the finite interface strengths tested. This is rather obvious, since these bounds are tighter than the Hill–Reuss–Voigt bounds for a true representative volume.

5. Conclusions

To an extent, the strong correlation found in the curve fits in Eq. (20), and the Plots in Fig. 11, lend credence to the so-called "1-D" models, where D, the damage variable, is the amount of open debonded interface area. This suggests that the amount of debonded surface area, if it could be determined, should serve as a primary "internal" variable in a homogenized macroscopic constitutive model for damage for this type of composite.

To an extent, the selection made in this paper of a critical stress for a failure criteria for debonding was too severe. Milder criteria, via more complex models, can also be incorporated within a unilateral constraint framework. Accordingly, we mention work in this area, which has concentrated on the failure of a single isolated interface. The fields between two dissimilar materials is a well explored subject dating back, at least, to the seminal paper of Williams [20]. Williams showed that the stress ahead of an interfacial crack is of the form $\sigma \sim r^{n-1/2+i\epsilon}$, where r is the radial the distance to the crack tip, n is an integer and ϵ is an "oscillation index" of the form:

$$\epsilon = \frac{1}{2\pi} \ln \left(\frac{\kappa_1/\mu_1 + 1/\mu_1}{\kappa_2/\mu_2 + 1/\mu_1} \right). \tag{22}$$

ϵ vanishes when the materials are the same, and the fields take on the well known form found in fracture mechanics literature. There have been many theoretical studies of the failure of a single interface, based on the work of Williams, using the Griffith criteria [21], by employing the *J-integral* concept of Cherepanov [22] and Rice [23]. For more on these approaches see Refs. [24–27]. Another approach is to realize that the elasticity solution produces singular values for the stress at the crack tip which is, of course, unrealistic. There is plasticized region in front of the crack, the *process zone*. During plastic deformation the crack tip is blunted. A candidate approach to "regularize" failure criteria is based on the classical work of Hill [28] for notched specimens (with finite notched radius). For plane strain and assuming a perfectly elastic–plastic solid with no work hardening, Hill's slip line field equation for the stress in the plastic zone ahead of a crack can be used immediately ahead of a blunted crack of radius ρ

$$\sigma \sim \sigma^{\mathrm{Y}} \left(\ln \left(1 + \frac{r}{\rho} \right) + \frac{1}{2} \right) \tag{23}$$

where σ^{Y} is the material's yield strength and ρ is the blunted crack tip radius. Qualitatively speaking, the stress rises quickly from σ^{Y} at the crack tip to $C \times \sigma^{\mathrm{Y}}, 1 < C < \infty$, at a short distance from the crack. Other possibly useful forms of regularization, in the context of contact problems with adhesion, are summarized in the recent work of Fremond [29].

In summary the following points are made: (1) The fibers interact in the debonding regime and incorporation of interactions are necessary to make accurate structural assessments. (2) For the chosen material microstructure and loading, approximately a group of at least 64 fibers in the transverse plane were needed to achieve stable results. (3) The loss in overall stiffness in the transverse direction can occur at infinitesmal applied displacements ($\beta = 0.002$). (4) The amount of debonded surface area is an extremely good indicator of the loss in overall stiffness in the transverse direction. (5) The nearly perfect correlation between the debonded micro-surface surface area and the loss in the macroscopic stiffness validates the use of the micro-surface area as an internal variable, in a possibly homogenized macroscopic model for damage.

To a large extent, the presented simulations have been possible because of the relatively recent rise in computing power and memory capacity of stand-alone workstations. However, 3-dimensional problems, for example a particulate problem with the same mesh density as used in our 2 dimensional simulations ($12 \times 12 \times 12$/particle), would require approximately 2,739,000 degrees of freedom. Without special techniques, such problems are beyond a direct simulation on a single workstation. There are various ways to approach such problems, for example with structural decomposition methods and Zohdi and Wriggers [30]. This method is based upon approximating local boundary data on a partition of the domain under analysis, thereby decomposing the structure into more computationally manageable subdomains. Other approaches, which are complementary to the structural decomposition involve local mesh adaptivity to save degrees of freedom. Specifically, in the context of contact problems, we mention the works of Carstensen et al. [31] and Wriggers et al. [9,13,32,33]. The incorporation of a computationally efficient failure criteria, involving a regularization of the unilateral debonding condition, in conjunction with structural decomposition and local adaptive mesh refinement, is a subject of current research of the authors.

References

[1] D. Krajcinovic, Damage Mechanics, North-Holland, Amsterdam, 1996.
[2] J. Lemaitre, J.-L. Chaboche, Mechanics of solid materials, Cambridge University Press, Cambridge, 1990.
[3] J. Lemaitre, Coupled elasto-plasticity and damage constitutive equations, Comp. Methods in Appl. Mech. Eng. 51 (1985) 31–49.
[4] J.P. Jones, W.J.S. Whittier, J. Appl. Mech. 34 (1967) 905.
[5] D.R.J. Owen, J.F. Lyness, Fiber Sci. Tech. 5 (1972) 129–141.
[6] J.I. Curikis, S. Valliappan, in: Ninth Australasian Conference on Mechanics and Structures of Materials, Sydney, Elsevier, Amsterdam, 1984, pp. 349–354.
[7] M.R. Winsom, J. Comp. Mater. 24 (1990) 707–726.
[8] S. Nutt, A. Needleman, Scripta Metall. 21 (1987) 705–710.
[9] P. Wriggers, J.C. Simo, A note on tangent stiffness for fully nonlinear contact problems, Comm. Appl. Num. Meth. 1 (1985) 199–203.
[10] G. Zavarise, R.L. Taylor, Point-to-segment contact geometry revisited, Joint Conference of Italian Group of Computational Mechanics and Ibero-Latin American Association of Computational Methods in Engineering, Padua, 1988, pp. 385–388.
[11] Z. Hashin, Analysis of composite materials: a survey, ASME J. Appl. Mech. 50 (1983) 481–505.
[12] J.R. Willis, The overall elastic response of composite materials, J. Appl. Mech. 50 (1983) 1202–1209.
[13] P. Wriggers, Finite element algorithms for contact problems, Archives of Computational Meth. Eng. 2 (4) (1995) 1–49.
[14] R. Hill, The elastic behaviour of a crystalline aggregate, Proc. Phys. Soc. A 65 (1952) 349–354.
[15] Z. Hashin, S. Shtrikman, On some variational principles in anisotropic and nonhomogeneous elasticity, J. Mech. Phys. Solids 10 (1962) 335–342.
[16] Z. Hashin, S. Shtrikman, A variational approach to the theory of the elastic behaviour of multiphase materials, J. Mech. Phys. Solids 11 (1963) 127–140.
[17] Z. Hashin, B.W. Rosen, The elastic moduli of fibre-reinforced materials, J. Appl. Mech. 31 (1964) 223–232.
[18] Z. Hashin, On elastic behavior of fibre-reinforced materials of arbitrary transverse phase geometry, J. Mech. Phys. Solids 13 (1965) 119–134.
[19] R. Hill, Theory of mechanical properties of fibre-strengthened materials-I. Elastic behaviour, J. Mech. Phys. Solids 12 (1964) 199–212.
[20] M. Williams, The stress around a fault or crack in dissimilar media, Bull. Seismological Soc. Amer. 49 (2) (1959) 199–204.
[21] A. Griffith, The phenomena of rupture flow in solids, Phil. Trans. Roy. Soc. London A 221 (1921) 163–197.
[22] G.P. Cherepanov, Crack propagation in continuous media, USSR J. Appl. Math. and Mech. Trans. 31 (1967) 504.
[23] J.R. Rice, A path independent integral and the approximate analysis of strain concentration by notches and cracks, J. Appl. Mech. (1968) 379–386.
[24] R.E. Smelser, M.E. Gurtin, On the J-integral for bi-material bodies, Int. J. Fracture 13 (1977) 382–384.
[25] J.W. Hutchinson, M.E. Mear, J.R. Rice, Crack paralleling an interface between dissimilar materials, J. Appl. Mech., Trans. ASME 54 (1987) 828–832.
[26] G.F. Shih, R.J. Asaro, Elastic-plastic analysis of cracks on bi-material interfaces. Part I. Small scale yielding, J. Appl. Mech., Trans. ASME 55 (1988) 299–313.

[27] J.R. Rice, Elastic fracture mechanics concepts for interfacial cracks, J. Appl. Mech., Trans. ASME 55 (1988) 98–103.
[28] R. Hill, The Mathematical Theory of Plasticity, Clarendon Press, Oxford, 1950.
[29] M. Fremond, Unilateral contact. Contact with Adhesion. Contact problems: Theory, Methods and Applications, CISM Lectures, Springer, Berlin, 1998.
[30] T.I. Zohdi, P. Wriggers, A domain decomposition method for bodies with microstructure based upon material regularization, The International Journal of Solids and Structures, accepted.
[31] C. Carstensen, O. Scherf, P. Wriggers, Numerical analysis for contact of elastic bodies, SIAM Sci. Comp., accepted.
[32] P. Wriggers, O. Scherf, An adaptive finite element algorithm for contact problems in plasticity, Computer Meth. Appl. Mech. Eng. 17 (1995) 88–97.
[33] P. Wriggers, O. Scherf, Adaptive finite element techniques for frictional contact problems involving large elastic strains, Computer Meth. Appl. Mech. Eng. 151 (1996) 593–603.